Aged hind-limb clasping experimental autoimmune encephalomyelitis models aspects of the neurodegenerative process seen in multiple sclerosis

Lindsay S. Cahill[a,1], Monan Angela Zhang[b,1], Valeria Ramaglia[b], Heather Whetstone[c], Melika Pahlevan Sabbagh[b], Tae Joon Yi[b], Laura Woo[a], Thomas S. Przybycien[b], Marina Moshkova[d], Fei Linda Zhao[b], Olga L. Rojas[b], Josephine Gomes[b], Stefanie Kuerten[e], Jennifer L. Gommerman[b], John G. Sled[a,f], and Shannon E. Dunn[b,d,g,h,2]

[a]Mouse Imaging Centre, The Hospital for Sick Children, Toronto, ON M5T 3H7, Canada; [b]Department of Immunology, University of Toronto, Toronto, ON M5S 1A8, Canada; [c]Peter Gilgan Centre for Research and Learning, Hospital for Sick Children, Toronto, ON M5G 0A4, Canada; [d]Toronto General Research Institute, University Health Network, Toronto, ON M5G 2C4, Canada; [e]Institute of Anatomy and Cell Biology, Friedrich-Alexander-Universität Erlangen-Nürnberg, 91054 Erlangen, Germany; [f]Department of Medical Biophysics, University of Toronto, Toronto, ON M5G 1L7, Canada; [g]Keenan Research Centre for Biomedical Science of St. Michael's Hospital, Toronto, ON M5B 1W8, Canada; and [h]Women's College Research Institute, Women's College Hospital, Toronto, ON M5S 1B2, Canada

Edited by Lawrence Steinman, Stanford University School of Medicine, Stanford, CA, and approved October 3, 2019 (received for review August 30, 2019)

Experimental autoimmune encephalomyelitis (EAE) is the most common model of multiple sclerosis (MS). This model has been instrumental in understanding the events that lead to the initiation of central nervous system (CNS) autoimmunity. Though EAE has been an effective screening tool for identifying novel therapies for relapsing-remitting MS, it has proven to be less successful in identifying therapies for progressive forms of this disease. Though axon injury occurs in EAE, it is rapid and acute, making it difficult to intervene for the purpose of evaluating neuroprotective therapies. Here, we describe a variant of spontaneous EAE in the 2D2 T cell receptor transgenic mouse (2D2^{+} mouse) that presents with hind-limb clasping upon tail suspension and is associated with T cell-mediated inflammation in the posterior spinal cord and spinal nerve roots. Due to the mild nature of clinical signs in this model, we were able to maintain cohorts of mice into middle age. Over 9 mo, these mice exhibited a relapsing-remitting course of hind-limb clasping with the development of progressive motor deficits. Using a combined approach of ex vivo magnetic resonance (MR) imaging and histopathological analysis, we observed neurological progression to associate with spinal cord atrophy, synapse degradation, and neuron loss in the gray matter, as well as ongoing axon injury in the white matter of the spinal cord. These findings suggest that mild EAE coupled with natural aging may be a solution to better modeling the neurodegenerative processes seen in MS.

multiple sclerosis model | neurodegeneration | progressive

Multiple sclerosis (MS) is an autoimmune disease that targets central nervous system (CNS) myelin and eventually causes progressive neurological disability in the majority of patients (1). Most patients with MS exhibit a relapsing-remitting form of disease from onset (1). MS relapses correlate with the appearance of white matter inflammatory demyelinating lesions that contain perivascular infiltrates of immune cells and blood–brain barrier (BBB) injury (2). Within 10 to 15 y, 70% of MS patients transition to secondary progressive MS (SPMS), which is characterized by a steady decline of neurological function (1, 3). In this stage of the disease, active demyelinating lesions with BBB breakdown become less frequent (2), cortical lesions become more prominent, and white and gray matter injury becomes more diffuse and spreads to the normal-appearing white and gray matter (3).

The major correlate of disability progression in MS is axon and neuronal loss (3). Although the pathological basis for neuron injury is not completely understood, there is strong evidence that it is linked to the ongoing inflammation in this disease (4, 5). In support of this notion, a major portion of CNS atrophy occurs within the white matter MS lesions (6), and axon injury within these lesions correlates with the number of infiltrating T cells and/or the activation of macrophage/microglia cells (4). In addition, the more diffuse axon injury seen in progressive MS has been shown to correlate to cortical lesion load and microglia activation (3). Infiltrating immune cells and activated microglia are thought to contribute to neuron damage via demyelination, axon transection, and secretion of immune products that mediate oxidative injury and mitochondrial dysfunction within neurons (2, 3, 5, 7–9). The disruption of axon transport in injured neurons and the degradation of neuronal synapses also affect the health of neighboring neurons (8, 10).

Experimental autoimmune encephalomyelitis (EAE) is a T cell-mediated autoimmune disease that shares pathological features with MS, including the formation of lymphocytic cuffs in the white matter and activation of BBB endothelium and submeningeal inflammation (11–13). This disease is commonly induced in inbred strains of mice via vaccination with protein components of myelin sheath emulsified with complete Freund's adjuvant (CFA) (14), but can also develop in mice that have been engineered to overexpress murine or human T cell receptors (TCRs) that are specific

Significance

EAE typically presents with hind-limb paralysis and is associated with severe T cell-mediated inflammation and axon injury throughout the spinal cord and parts of the brain. Because axon loss is so rapid in this model, it is difficult to intervene for the purpose of evaluating neuroprotective therapies. Here we describe a mild form of EAE that does not even meet the threshold for scoring on traditional EAE scales, yet with age results in devastating neurodegenerative changes in the spinal cord, including grey matter atrophy, neuron loss, and synapse degradation. These observations underscore the utility of T cell receptor transgenic mice to study the effect of natural aging on CNS autoimmunity and neurodegeneration.

Author contributions: L.S.C., V.R., O.L.R., J.L.G., J.G.S., and S.E.D. designed research; L.S.C., M.A.Z., V.R., H.W., M.P.S., T.J.Y., L.W., T.S.P., M.M., F.L.Z., O.L.R., J.G., and S.E.D. performed research; J.G.S. contributed new reagents/analytic tools; L.S.C., M.A.Z., V.R., T.J.Y., L.W., S.K., and S.E.D. analyzed data; and L.S.C., T.J.Y., J.L.G., and S.E.D. wrote the paper.

The authors declare no competing interest.

This article is a PNAS Direct Submission.

[1]L.S.C. and M.A.Z. contributed equally to this work.

[2]To whom correspondence may be addressed. Email: Shannon.Dunn@unityhealth.to.

This article contains supporting information online at www.pnas.org/lookup/suppl/doi:10.1073/pnas.1915141116/-/DCSupplemental.

First published October 22, 2019.

to myelin antigens (15–20). Though EAE has been successfully employed to study the mechanisms of action of certain disease-modifying therapies in MS, this model has proven to be less successful in identifying therapies for progressive MS. Axon injury is very rapid and acute in EAE, making it difficult to intervene for the purpose of evaluating neuroprotective therapies. For example, in myelin oligodendrocyte glycoprotein peptide 35-55 (MOG p35-55)/CFA-induced EAE in C57BL/6 mice, axon numbers decrease by 15% even prior to the onset of acute signs and by 60% at 1 mo postonset of EAE (21). The severe nature of paralytic symptoms in this model also makes it difficult to ethically justify long-term studies to study how neurodegenerative processes mature with age.

Here, while exploring the role of the nuclear receptor peroxisome proliferator-activated receptor alpha (PPARα) on the incidence of autoimmunity in $2D2^+$ mice, we made the serendipitous observation that $2D2^+$ mice in our specific pathogen-free (SPF) colony often exhibited hind-limb clasping upon tail suspension. The onset of this abnormal reflex was associated with the development of T cell inflammation and axon injury in the posterior spinal cord. Because of the mild nature of this disease, we were able to maintain cohorts of $2D2^+$ mice in good health into middle age, when we observed these mice to develop progressive motor deficits. This phenotype was associated with spinal cord atrophy, ongoing axon injury in the white matter, and neuron loss and synapse degradation in the gray matter of the spinal cord. These findings suggest that mild EAE coupled with natural aging may be a solution to modeling the neuronal degeneration seen in SPMS.

Results

Hind-limb Clasping in $2D2^+$ Mice and Modulation by PPARα Deficiency. We previously reported that male, but not female, mice that were homozygotes for a mutant PPARα allele ($PPAR\alpha^{mut/mut}$) developed a hyperacute form of EAE with enhanced Th1 inflammation upon immunization with MOG p35-55/CFA, suggesting a male-specific role for PPARα in limiting Th1 inflammation during EAE (22). However, these studies did not resolve whether this protein regulates the incidence of CNS autoimmunity, since all mice developed disease in this model (22). To address this aspect, we acquired $PPAR\alpha^{mut/mut}$ mice on the C57BL/6 background from Taconic Farms, crossed these mice with $2D2^+$ mice obtained from Jackson Laboratory, and then monitored clinical signs in parental, F1, and F2 $2D2^+$ mice until 20 wk of age.

It has been previously reported that $2D2^+$ mice develop spontaneous EAE with low incidence (0 to 20%) when housed under SPF conditions (16, 23–26). We observed EAE incidence to be higher in our $2D2^+$ colony, with ∼25% of mice developing classic EAE signs including tail and hind-limb paralysis (Table 1). When classic EAE occurred, it presented between 4 and 8 wk of age with severe and ascending paralysis (Table 1 and *SI Appendix*, Fig. S1*A*). If mice survived past this age without developing EAE, they often presented with a positive hind-limb clasping reflex upon tail suspension (*SI Appendix*, Fig. S1 *B–D* and Table 1). This neurological sign has been described in certain murine models of neurodegeneration (i.e., Huntington's disease, Alzheimer's, Rett's syndrome [27]) and as a prelude to tail paralysis in certain EAE models (28). Interestingly, when examining the phenotype of the $2D2^+$ mice that were wild-type for PPARα (parental $2D2^+$ and $PPAR\alpha^{WT/WT}$ F2 $2D2^+$ colonies), we observed clinical signs to develop more frequently in females ($\chi^2 = 17.1$, $P < 0.00001$; Table 1 and *SI Appendix*, Fig. S1*E*). Male, but not female, $2D2^+$ mice with PPARα deficiency ($PPAR\alpha^{mut/mut}$ and $PPAR\alpha^{mut/WT}$ genotypes) exhibited a higher incidence of clinical signs than $PPAR\alpha^{WT/WT}$ $2D2^+$ counterparts ($\chi^2 = 18.82$, $P = 0.000082$; Table 1). Together, these findings supported a sex-dependent role for PPARα in regulating the incidence of CNS autoimmunity and revealed hind-limb clasping as a prominent clinical sign in $2D2^+$ mice.

The Onset of Hind-limb Clasping Associates with the Development of Mild T Cell Inflammation in the Posterior Spinal Cord. Since hind-limb clasping had not yet been characterized in EAE to our awareness, we conducted further studies to understand the pathological basis of this phenotype. We intercrossed $PPAR\alpha^{mut/WT}$ F2 $2D2^+$ offspring to maintain the line and further characterized the hind-limb clasping phenotype in $PPAR\alpha^{mut/WT}$ $2D2^+$ female offspring for the reasons that 1) this was the most frequent genotype generated by our breeding strategy, 2) the genotype did not

Table 1. Incidence and age of onset of paralysis and hind-limb clasping in parental breeder, F1, and F2 colonies of $2D2^+$ mice over a 20 wk observation period

Groups	N	Classic EAE, %	Hind-limb clasping, %	No symptoms, %	Age of onset classic EAE, wk	Age of onset hind-limb clasping, wk
Male						
Parental $2D2^+$ mice	38	26.3	39.4	34.3	n.r.	n.r.
F1 ($PPAR\alpha^{mut/WT}$ $2D2^+$)	19	11	68.4	20.6	n.r.	n.r.
F2 ($PPAR\alpha^{WT/WT}$ $2D2^+$)	29	17.2	48.3	34.5	6.2 (0.5)	7.5 (0.5)
F2 ($PPAR\alpha^{mut/WT}$ $2D2^+$)	14	21.4	64.3	14.3*	6.3 (0.7)	5.9 (0.5)
F2 ($PPAR\alpha^{mut/mut}$ $2D2^+$)	23	26.0	60.9	13.1*	6.8 (0.9)	8.0 (1.5)
Female						
Parental $2D2^+$ mice	49	32.6	58.3	9.1	n.r.	n.r.
F1 ($PPAR^{mut/WT}$ $2D2^+$)	20	30	70.0	0	n.r.	n.r.
F2 ($PPAR\alpha^{WT/WT}$ $2D2^+$)	19	42.1	57.9	0	6.0 (0.2)	8.3 (0.8)
F2 ($PPAR\alpha^{mut/WT}$ $2D2^+$)	21	28.6	66.7	4.7	7.0 (0.7)	7.0 (0.7)
F2 ($PPAR\alpha^{mut/mut}$ $2D2^+$)	25	41.6	54.2	4.2	6.4 (0.5)	6.9 (0.6)

Parental $2D2^+$ mice that were homozygotes for the T cell receptor (TCR) transgene and were obtained from the Jackson Laboratory. These mice were crossed with mice that were homozygotes for a mutant (mut) form of PPARα ($PPAR\alpha^{mut/mut}$ mice) that are missing the ligand-binding domain of the receptor (obtained from Taconic Farms) to generate F1 offspring that had one copy of the TCR transgene, one copy of the $PPAR\alpha^{mut}$ allele, and one copy of the wild-type (WT) PPARα allele ($PPAR\alpha^{mut/WT}$). F1 offspring were intercrossed to generate F2 pups that were screened for the presence $PPAR\alpha^{WT}$ and $PPAR\alpha^{mut}$ alleles by PCR and for the presence of the 2D2 TCR transgene ($2D2^+$) by flow cytometry. Mice of each type were monitored twice weekly from weaning until 20 wk of age for the development of clinical signs. Hind-limb clasping was defined as the occurrence of clasping of one or both limbs upon tail suspension. Classic EAE was defined as the occurrence of tail or hind-limb paralysis. Note that mice designated as hind-limb clasping or having no symptoms did not develop classic EAE signs. Hind-limb clasping was first noted in the parental $2D2^+$ and F1 colonies and record keeping for the occurrence of these signs is not as reliable (n.r.) and therefore is not presented. n = number of mice in each group.
*Different from $PPAR\alpha^{WT/WT}$ $2D2^+$ male by χ^2 test.

influence disease incidence in this sex (Table 1), and 3) females were easier to maintain than males due to less infighting.

First, we examined the pathology in the spinal cord and brain of female PPARα$^{mut/WT}$ 2D2^{+} mice that had started clasping 3 to 4 d previously and an equal number of PPARα$^{mut/WT}$ 2D2^{+} mice that had instead developed classic EAE signs (n = 8 mice per group). Spinal cord and brains were sectioned and stained with Luxol fast blue/hematoxylin and eosin (LFB/H&E) and anti-CD3 to visualize inflammatory demyelinating lesions and SMI-32 antibody to detect injured axons. In the hind-limb clasping-onset mice, the most frequent observation was mild T cell inflammation in the posterior spinal cord (Figs. 1*A* and 2 *A*, *C*, and *G*). This T cell infiltration associated with microglia activation and axon injury (Fig. 2 *B* and *D* and *SI Appendix*, Fig. S2 *A*–*C*). By contrast, PPARα$^{mut/WT}$ 2D2^{+} mice that succumbed to classic EAE signs displayed higher inflammation scores (Fig. 1*E*) and more severe T cell inflammation (Fig. 2*E*), axonal injury (Fig. 2*F*), and myelin loss (Fig. 1*F*). Mice with classic EAE had T cell infiltrates that were equally distributed between ventral, dorsal, and lateral aspects of the cord (Fig. 2*G*).

Consistent with past studies of 2D2^{+} mice, immune cell infiltration was also detected in the spinal nerve roots (Fig. 1 *C* and *D*) (29) and in the optic nerves or optic tract (*SI Appendix*, Fig. S2*D*) (16), but was otherwise infrequent in the brain in PPARα$^{mut/WT}$ 2D2^{+} mice (i.e., 2.3 ± 0.5 inflammatory foci per brain with hind-limb clasping, 4.3 ± 1.6 foci per brain in mice with classic EAE; P = 0.25 by 2-tailed Mann–Whitney U test, n = 8 mice per group). Other than the optic tract, brain inflammatory foci were detected in the corpus callosum (3 of 8 mice), the cerebellum (1 of 8 mice), the cerebral peduncle (1 of 8 mice), the inferior colliculus (1 of 8 mice), and the spinal tract of the trigeminal nerve (2 of 8 mice). We did note significant submeningeal inflammation, which consisted of aggregates of T and B cells, in 1 mouse with clasping-onset EAE (*SI Appendix*, Fig. S2 *E* and *F*). This pathological feature has been previously described in 2D2^{+} mice crossed onto the MOG B cell receptor knock-in background and to associate with severe EAE development (30). Consistent with this, we observed submeningeal inflammation to be more prevalent in PPARα$^{mut/WT}$ 2D2^{+} mice that developed classic EAE signs (Fig. 1*H*). Taken together, these findings suggest that hind-limb clasping in PPARα$^{mut/WT}$ 2D2^{+} mice was caused by T cell infiltration in the posterior spinal cord and/or nerve roots.

Hind-limb Clasping EAE Starts as a Relapsing-Remitting Disease But Is Associated with the Progressive Development of Motor Deficits with Age. While monitoring our F1 and F2 generation 2D2^{+} breeding females with age, we noted that hind-limb clasping waxed and waned in young adulthood; the remissions from clasping in breeding females often coincided with pregnancy, whereas clasping scores worsened postpartum (*SI Appendix*, Fig. S3). This recovery from clasping corresponded pathologically with the presence of mild perivascular inflammation (*SI Appendix*, Fig. S2*G*), demyelination (*SI Appendix*, Fig. S2*H*), or atypical vacuolar structures in the posterior spinal cord (*SI Appendix*, Fig. S2*I*), which we speculate could be remnants of a submeningeal inflammatory process. We had also observed that, with age, hind-limb clasping signs progressed in severity, transitioning from a mild clasping phenotype in one or both feet (Movie S1 and *SI Appendix*, Fig. S1*C*) to a more severe and sustained form of clasping in both feet (Movie S2 and *SI Appendix*, Fig. S1*D*).

To better capture this disease progression in PPARα$^{mut/WT}$ 2D2^{+} mice, we developed a scoring system for hind-limb clasping and followed an additional cohort of 14 female PPARα$^{mut/WT}$ 2D2^{+} mice and 15 sex-matched PPARα$^{mut/WT}$ 2D2^{-} littermate controls from weaning until 9 mo of age. Five of the PPARα$^{mut/WT}$ 2D2^{+} mice developed classic EAE shortly after weaning and were killed, and the remaining 9 PPARα$^{mut/WT}$ 2D2^{+} and 15 PPARα$^{mut/WT}$ 2D2^{-} mice were observed for clinical signs. When

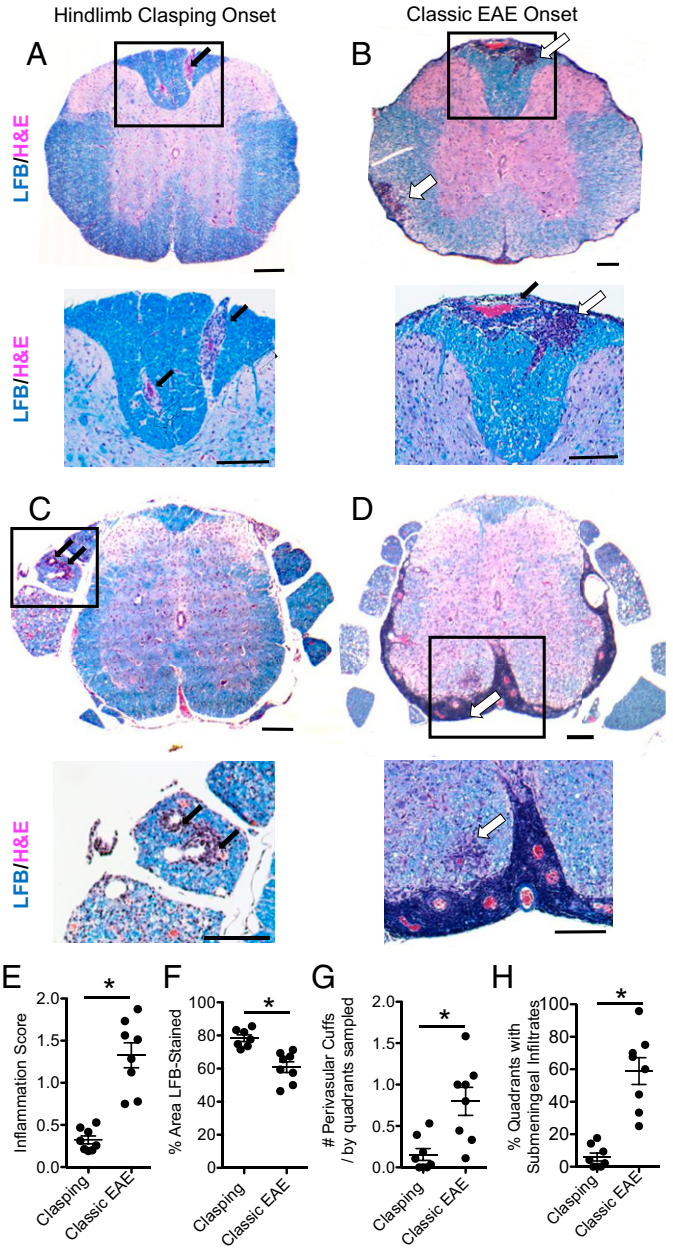

Fig. 1. Hind-limb clasping is a mild form of EAE. PPARα$^{mut/WT}$ 2D2^{+} mice were examined for the first development of hind-limb clasping (*A* and *C*) or classic EAE signs (*B* and *D*). Three to 4 days postonset, spinal cords and brains were harvested from mice and embedded in paraffin. Cross-sections of the spinal cord (n = 8 mice per group) were cut and stained with Luxol fast blue/H&E (*A*–*D*). Representative images of the thoracic (*A* and *B*) or sacral (*C* and *D*) spinal cord from mice with hind-limb clasping-onset (*A* and *C*) or classic EAE-onset (*B* and *D*). (Scale bars: *Top*, 200 μm; *Bottom*, 100 μm.) Black arrows point to perivascular cuffs. Open arrows point to areas of parenchymal inflammation in the CNS white matter. (*E*–*H*) Scoring of the inflammation and demyelination in LFB/H&E-stained sections. (*E*) Inflammation score. (*F*) Percent area of white matter that was positive for LFB staining at the level of the thoracic cord. (*G*) Number of perivascular cuffs/no. of quadrants sampled. (*H*) Percentage of quadrants that had submeningeal immune cell infiltrates. *Different between groups as assessed by Mann–Whitney U test (2-tailed). Values are means ± SEM. Symbols represent individual mice.

examining individual mice, the majority (8 of 9) of mice in the PPARα$^{mut/WT}$ 2D2^{+} group exhibited a relapsing-remitting course of hind-limb clasping in young adulthood (examples of individual mice shown in Fig. 3*A*); however, on average,

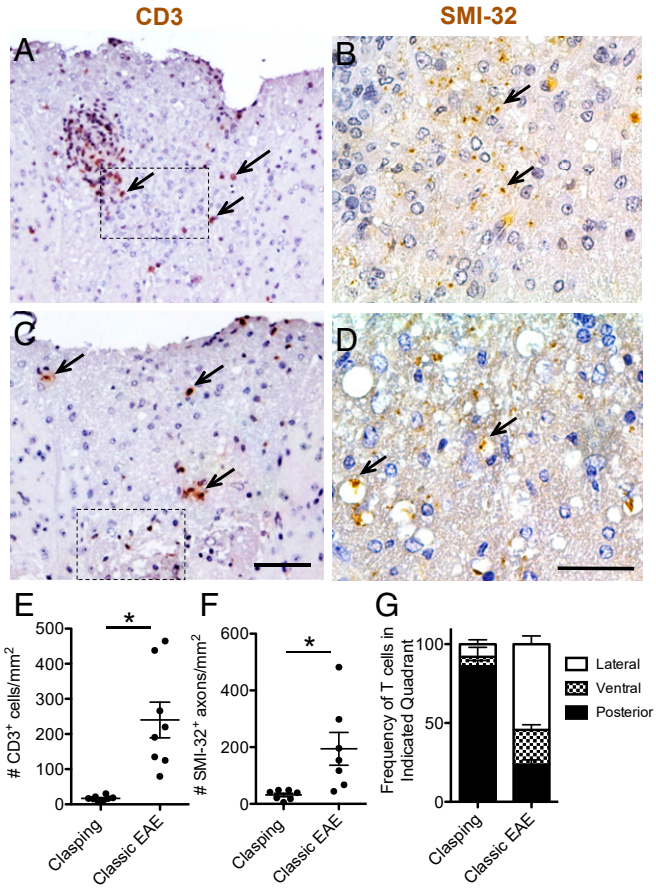

Fig. 2. Hind-limb clasping is characterized by mild T cell infiltration in the posterior spinal cord. Cross-sections taken at the level of the thoracic cord were stained with CD3 (200×; *A* and *C*) or SMI-32 (400×; *B* and *D*) antibodies to detect T cells or injured axons. (*A–D*) Severe (*A* and *B*) and mild (*C* and *D*) examples of T cell infiltration seen in hind-limb clasping mice. Arrows point to some positively stained T cells (*Left*) or SMI-32$^+$ axons (*Right*). (Scale bars: *A* and *C*, 100 μm; *B* and *D*, 50 μm.) Hatched-line rectangles in *A* and *C* indicate the approximate location of the areas of SMI-32 staining in the adjacent section shown in *B* and *D*. (*E*) Number of CD3$^+$ T cells per square millimeter white matter sampled. (*F*) Number of SMI-32$^+$ axons per square millimeter white matter. *Different between groups as assessed by Mann–Whitney *U* test (2-tailed). Values in the graphs represent individual mice. (*G*) Frequency of total CD3$^+$ T cells that were present in the anterior, posterior, or 2 lateral quadrants (pooled together) in the spinal cord. Values are mean ± SEM frequencies determined for individual mice (n = 8 per group).

clasping scores worsened with age (Fig. 3*B*). By contrast, PPARα$^{mut/WT}$ 2D2$^-$ littermates remained asymptomatic throughout (Fig. 3*B*).

To evaluate motor deficits in these mice, we also subjected both groups of mice to a rotarod task and a hanging grip test at 3, 6, and 9 mo of age. When compared to PPARα$^{mut/WT}$ 2D2$^-$ mice, PPARα$^{mut/WT}$ 2D2$^+$ mice exhibited shorter times to fall on the rotarod at 6 and 9 mo of age (Fig. 3*C*) and exhibited profound impairments in the hanging grip test at all ages examined (Fig. 3*D*). Though 3 PPARα$^{mut/WT}$ 2D2$^+$ mice had to be killed due to lymphoma development between 6 and 8 mo of age, the 6 PPARα$^{mut/WT}$ 2D2$^+$ mice that survived to the 9-mo endpoint exhibited similar body weights as age-matched littermate PPARα$^{mut/WT}$ 2D2$^-$ controls (PPARα$^{mut/WT}$ 2D2$^-$: 24.8 ± 1.6 g, n = 15; vs. PPARα$^{mut/WT}$ 2D2$^+$, 24.2 ± 2.8 g, n = 6; P = 0.69 by 2-tailed t test), indicating that these mice were in reasonably good health at the study endpoint.

Neurological Progression with Age in PPARα$^{mut/WT}$ 2D2$^+$ Mice Is Not Due to Increased Autoimmune Inflammation. The gradual worsening in performance on rotarod and hanging grip tasks suggested either that CNS autoimmunity had escalated or that neuron damage had accumulated with age in PPARα$^{mut/WT}$ 2D2$^+$ mice. To further examine this, we conducted MR imaging on fixed spinal cords and brains collected from 9-mo-old PPARα$^{mut/WT}$ 2D2$^+$ females and age-matched PPARα$^{mut/WT}$ 2D2$^-$ littermate controls postinfusion with gadolinium contrast (representative images in Fig. 4 *A* and *B*). This analysis revealed areas of hyperintensity in 3-dimensional T2-weighted (3D T2w) MR images of the spinal cord, but not brain, in 3 of 5 PPARα$^{mut/WT}$ 2D2$^+$ and in none of the PPARα$^{mut/WT}$ 2D2$^-$ mice examined. In 2 PPARα$^{mut/WT}$ 2D2$^+$ cases, areas of hyperintensity corresponded with the presence of similar vacuolar structures as seen in mice that had recovered from clasping (e.g., Fig. 4 *A–C*). In another case, the area of hyperintensity mapped to a focus of T cell infiltration in the lateral lumbar spinal cord (Fig. 4 *D–F*). To see if the MR had missed mild T cell infiltration, we conducted a more detailed survey for CD3$^+$ T cells in spinal cord sections of these same mice by IHC. This analysis revealed very few T cells in the spinal cord of aged PPARα$^{mut/WT}$ 2D2$^+$ mice, and the numbers of T cells evaluated per section did not significantly differ from that in PPARα$^{mut/WT}$ 2D2$^-$ controls (1.1 ± 0.4 in PPARα$^{mut/WT}$ 2D2$^-$ mice, 2.0 ± 0.4 in PPARα$^{mut/WT}$ 2D2$^+$ mice; P = 0.18 by 2-tailed t test, n = 5 per group). We also evaluated inflammation and demyelination on LFB/H&E sections in an additional 5 PPARα$^{mut/WT}$ 2D2$^+$ and 5 PPARα$^{mut/WT}$ 2D2$^-$ cases that had been followed for 9 mo but had not been imaged by MR. We observed that only 1 of the PPARα$^{mut/WT}$ 2D2$^+$ mice showed evidence of ongoing inflammation, with a focus of submeningeal inflammation detected in the spinal cord (Fig. 4*G*) and small perivascular cuffs detected in the cerebellum (Fig. 4*H*) and the cerebral peduncle (Fig. 4*I*). These findings suggest that inflammatory activity in the spinal cord is more sporadic in PPARα$^{mut/WT}$ 2D2$^+$ mice with age.

T Cell Autoimmunity Subsides with Age in PPARα$^{mut/WT}$ 2D2$^+$ Mice. To better understand the underlying basis for the abatement of Th autoimmunity in PPARα$^{mut/WT}$ 2D2$^+$ mice with age, we conducted an exploratory immune study on an additional cohort of 7- to 9-mo-old PPARα$^{mut/WT}$ 2D2$^+$ (n = 6 mice) and PPARα$^{mut/WT}$ 2D2$^-$ (n = 9 mice). Similar to previous studies (31), we detected CD4$^+$ T cells to be more abundant in PPARα$^{mut/WT}$ 2D2$^+$ mice (*SI Appendix*, Fig. S5). Further, TCR transgenic CD4$^+$ T cells (identified by TCR Vβ11.1$^+$ staining) had stronger reactivity toward an epitope on neurofilament medium (NF-M) compared to MOG peptide and primarily produced IFN-γ and with a lower frequency of cells coproducing GM-CSF or IL-17 (*SI Appendix*, Fig. S4). When contrasted with total CD4$^+$ T cells from PPARα$^{mut/WT}$ 2D2$^-$ mice or nontransgenic CD4$^+$ T cells from the PPARα$^{mut/WT}$ 2D2$^+$ mice, TCR transgenic CD4$^+$ T cells exhibited reduced expressions of the T cell activation marker CD25 and the exhaustion marker PD-1, and were less likely to be CD25$^+$FoxP3$^+$ T regulatory cells (*SI Appendix*, Fig. S5), suggesting that these cells were in a quiescent state. When compared with TCR Vβ11.1$^+$ CD4$^+$ T cells in the PPARα$^{mut/WT}$ 2D2$^-$ mice, TCR transgenic CD4$^+$ T cells in the 2D2$^+$ mice in the cervical lymph node exhibited down-regulated TCRβ expression (*SI Appendix*, Fig. S5), which has been described as a mechanism of clonal anergy in self-antigen–specific TCR systems (32, 33). We also observed an enrichment in T regulatory cells in the nontransgenic CD4$^+$ T pool in the same lymph nodes (*SI Appendix*, Fig. S5). Since Tregs are known to limit CNS autoimmunity in 2D2$^+$ mice (16), these findings suggested that the attenuation of T cell autoimmunity with aging in 2D2$^+$ mice was due to peripheral tolerance mechanisms.

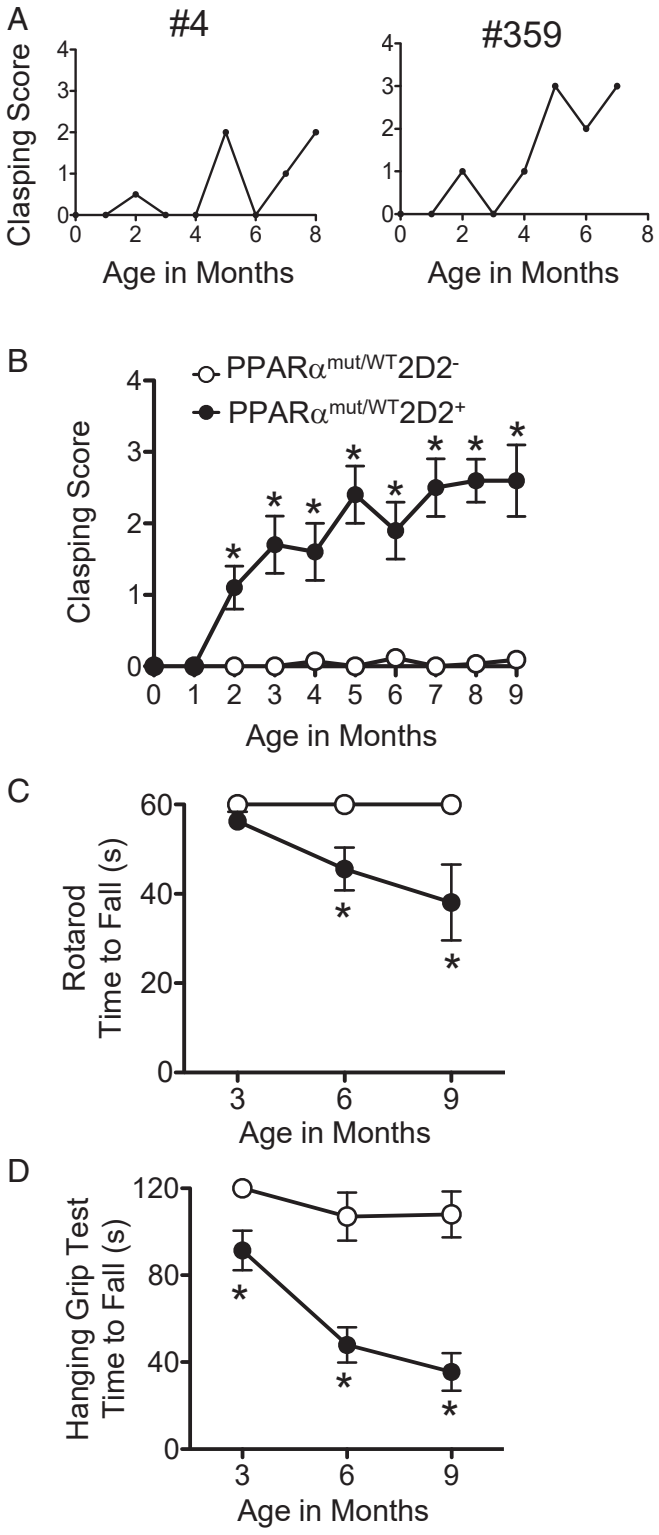

Fig. 3. Neurological progression with age in PPARα$^{mut/WT}$ 2D2^{+} mice that presented with hind-limb clasping. A cohort of 14 PPARα$^{mut/WT}$ 2D2^{+} and 15 PPARα$^{mut/WT}$ 2D2^{-} mice were followed for clinical signs of clasping until 9 mo of age. Five PPARα$^{mut/WT}$ 2D2^{+} mice developed classic EAE signs and were excluded from this analysis; however, scores for an additional 3 mice that developed hind-limb clasping but died from lymphoma ($n = 3$) were included up until time of death. (*A*) Examples of hind-limb clasping scores in individual PPARα$^{mut/WT}$ 2D2^{+} mice with age. (*B*) Mean ± SEM of clinical scores in a cohort of PPARα$^{mut/WT}$ 2D2^{+} mice ($n = 9$) and littermate PPARα$^{mut/WT}$ 2D2^{-} controls ($n = 15$) up until 9 mo of age. For this analysis, scores for individual mice (collected 1 to 2 times per week) were averaged for each month of life. (*C* and *D*) Mean ± SEM times to fall on a fixed-speed (32 rpm) rotarod task (*C*) or a hanging grip test (*D*) that was performed at 3, 6, and 9 mo of age. For the rotarod test, the value for each individual mouse is the longest time to fall recorded for 3 trials. For the hanging grip test, the value for each individual mouse is the average time to fall for 3 trials. *Significantly different from PPARα$^{mut/WT}$ 2D2^{-} control by Mann–Whitney *U* test (2-tailed) ($P \leq 0.05$).

Since B cell-mediated pathogenic mechanisms have been implicated in progressive MS (34, 35), we also evaluated the B cell compartment and measured autoantibody levels in aged PPARα$^{mut/WT}$ 2D2^{+} and PPARα$^{mut/WT}$ 2D2^{-} mice. We detected a tendency for an increased number of B cells in the cervical lymph nodes of PPARα$^{mut/WT}$ 2D2^{+} vs. PPARα$^{mut/WT}$ 2D2^{-} mice, an effect that was driven by an increase in the frequency of follicular B cells, a subset that specializes in T cell-dependent antibody production (*SI Appendix*, Table S1). Consistent with this finding, we detected the levels of MOG-, NF-M–, and MP4- (PLP/MBP fusion protein) specific IgG1 to be elevated in the serum of PPARα$^{mut/WT}$ 2D2^{+} mice (*SI Appendix*, Fig. S8*A*). Since MOG-specific IgG1 antibodies have been shown to fix complement and promote inflammation and demyelination in EAE (36), we probed CNS sections of aged PPARα$^{mut/WT}$ 2D2^{+} and PPARα$^{mut/WT}$ 2D2^{-} mice ($n = 10$ per group) with anti-mouse IgG, but detected no positive staining in the spinal cord parenchyma in any of the mice that we examined (*SI Appendix*, Fig. S8 *B–D*). These findings suggested a disconnect between autoimmune mechanisms and disease progression in 2D2^{+} mice with age.

MRI Correlates of Neurological Progression. Since T cell autoimmunity declined with age, we turned our attention to neurodegenerative mechanisms as a cause of the progressive motor deficits in PPARα$^{mut/WT}$ 2D2^{+} mice. One major correlate of neurological progression in MS is atrophy of the brain and spinal cord. Therefore, we evaluated spinal cord and whole brain volume in our 9-mo-old PPARα$^{mut/WT}$ 2D2^{+} and PPARα$^{mut/WT}$ 2D2^{-} mice imaged by MR. This analysis revealed significant atrophy of the spinal cord, but not the brain, in aged PPARα$^{mut/WT}$ 2D2^{+} mice (Fig. 5 *A–D*). This was accompanied by the appearance of a hyperintense rim of contrast around the cord (Fig. 5*B*), which we speculate was due to the accumulation of contrast agent in the increased space around the spinal cord postfixation. This loss in total spinal cord volume in PPARα$^{mut/WT}$ 2D2^{+} mice was driven by both gray and white matter loss, but only the former was significant (Fig. 5 *E* and *F*).

PPARα$^{mut/WT}$ 2D2^{+} Mice Exhibit a Loss of Axons and Ongoing Axonal Injury in the White Matter. To better understand the basis for tissue loss in the white matter, we stained representative sections from the thoracic cord of PPARα$^{mut/WT}$ 2D2^{+} and PPARα$^{mut/WT}$ 2D2^{-} mice with LFB/H&E to detect inflammatory demyelinating lesions and SMI-32 to detect injured axons. We did not observe any areas with gross demyelination on LFB-stained sections, but did observe the presence of larger vacuoles in the white matter of the PPARα$^{mut/WT}$ 2D2^{+} compared to PPARα$^{mut/WT}$ 2D2^{-} mice, which was suggestive of axon loss (Fig. 6*B* vs. Fig. 6*A*). To specifically evaluate this, we preserved spinal cords from an additional three 9- to 11-mo PPARα$^{mut/WT}$ 2D2^{+} mice and PPARα$^{mut/WT}$ 2D2^{-} controls in resin and counted axons in thin sections of the dorsal spinal cord (level of the thoracic spine) that had been stained with toluidine blue (*SI Appendix*, Fig. S9). This analysis revealed that the number of axons was significantly reduced in PPARα$^{mut/WT}$ 2D2^{+} compared to PPARα$^{mut/WT}$ 2D2^{-} mice (*SI Appendix*, Fig. S9*B*). To evaluate the structural integrity of myelinated axons, we also conducted a transmission electron microscopy (TEM) study of the dorsal spinal cord in these same mice. This analysis revealed signs of early axonal degeneration in

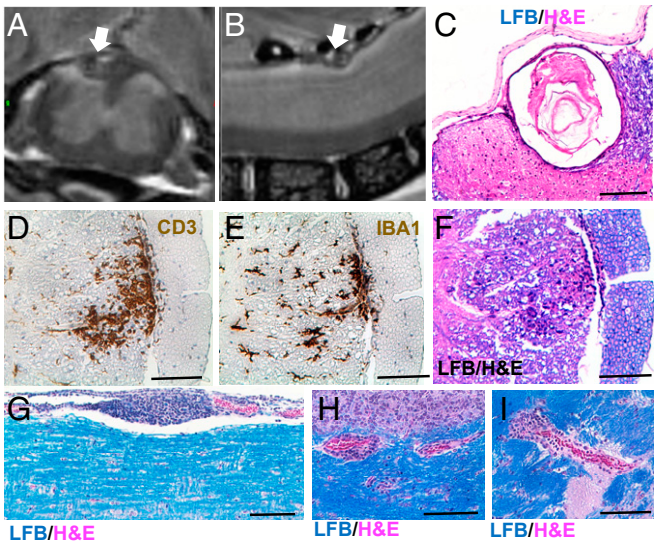

Fig. 4. CNS inflammation is more sporadic with age in long-term clasping PPARα$^{mut/WT}$ 2D2^{+} mice. PPARα$^{mut/WT}$ 2D2^{+} females and sex-matched PPARα$^{mut/WT}$ 2D2^{-} littermates (n = 5 mice per group) from the study in Fig. 3 were transcardially perfused with gadolinium and PFA fixative at 9 mo of age. Fixed spinal cord and brain specimens were then harvested for MR imaging within bone and then were decalcified, embedded in paraffin, and sectioned for histological analysis of inflammation. (*A* and *B*) Area of hyperintensity (designated by a white arrow) on a T2-weighted image of the spinal cord in 1 PPARα$^{mut/WT}$ 2D2^{+} mouse in cross-section (*A*) or longitudinal (*B*) views. (*C*) The same structure in paraffin sections prepared from the imaged cord stained with LFB/H&E. (*D*–*F*) One focus of inflammation corresponded to an area of hyperintensity in another PPARα$^{mut/WT}$ 2D2^{+} mouse stained with anti-CD3 (*D*), anti-IBA1 (*E*), or LFB/H&E (*F*). (*G*–*I*) Example of submeningeal inflammation in the spinal cord (*G*) and small perivascular cuffs in the cerebellum (*H*) or cerebral peduncle (*I*) in another PPARα$^{mut/WT}$ 2D2^{+} mouse of similar age that had not been imaged by MR. (Scale bar, 100 μm.)

PPARα$^{mut/WT}$ 2D2^{+} mice, characterized by a loss of the central axon and a collapse of the myelin sheath (*SI Appendix*, Fig. S9*D*). No immune cells were imaged in close proximity to these injured axons. These TEM findings of ongoing axon injury also aligned with our finding of an increased number of SMI-32^{+} axons per square millimeter in the dorsal spinal cord of PPARα$^{mut/WT}$ 2D2^{+} compared to age-matched PPARα$^{mut/WT}$ 2D2^{-} mice (Fig. 6 *C*, *D*, and *I*). To evaluate whether the axon injury colocalized with microglia activation, we stained adjacent paraffin sections for the microglia marker ionized calcium binding adaptor molecule 1 (IBA1). In areas where we observed only a few axons positive for SMI-32^{+}, microglia in adjacent sections resembled those in PPARα$^{mut/WT}$ 2D2^{-} mice, whereas, in cases where a higher number of SMI-32^{+} axons were present, microglia stained more darkly with IBA1 antibody, consistent with a more reactive phenotype (*SI Appendix*, Fig. S10).

Gray Matter Changes in PPARα$^{mut/WT}$ 2D2^{+} Mice with Age. To determine the pathological substrate for gray matter atrophy in 9-mo-old PPARα$^{mut/WT}$ 2D2^{+} mice, we stained and then counted the number of NeuN^{+} neuronal nuclei in a set volume of gray matter tissue in the thoracic spinal cord using the optical fractionator technique (37, 38). We observed that PPARα$^{mut/WT}$ 2D2^{+} mice exhibited a significant reduction in the number of NeuN^{+} neurons in the gray matter compared to age-matched PPARα$^{mut/WT}$ 2D2^{-} controls (Fig. 6*J*). We detected no difference in these numbers after normalizing to the volume of tissue sampled (Fig. 6*K*), indicating neuronal loss was the cause of gray matter atrophy in the spinal cord.

Another pathological correlate of progressive MS is degradation of neuronal synapses (39, 40). Siponimod, a drug that has had significant effects in slowing disease progression in a subgroup of SPMS patients (41), has been shown to improve synaptic dysfunction in preclinical models (42), highlighting the potential importance of this pathological feature to disease progression. To gain insights into synaptic integrity in spinal cord neurons in PPARα$^{mut/WT}$ 2D2^{+} mice, we stained thoracic sections from 9-mo-old PPARα$^{mut/WT}$ 2D2^{+} and PPARα$^{mut/WT}$ 2D2^{-} mice for the presynaptic marker synaptotagmin (Fig. 6 *G* and *H*). This analysis revealed a decrease in synaptotagmin-positive synapses in the spinal cord of PPARα$^{mut/WT}$ 2D2^{+} compared to PPARα$^{mut/WT}$ 2D2^{-} mice (Fig. 6*L*), indicating that synaptic loss occurred in PPARα$^{mut/WT}$ 2D2^{+} mice with age.

Region-Specific Brain Atrophy in PPARα$^{mut/WT}$ 2D2^{+} Mice. Though the whole brain was not atrophied in aged PPARα$^{mut/WT}$ 2D2^{+} mice (Fig. 5*D*), the finding of degraded synapses in the spinal cord made us question whether there could be atrophy of brain structures that contain neurons that connect with those in the posterior columns of the spinal cord. We therefore measured the volumes of 62 different brain substructures in acquired 3D MRI images. This analysis revealed a significant decrease in the

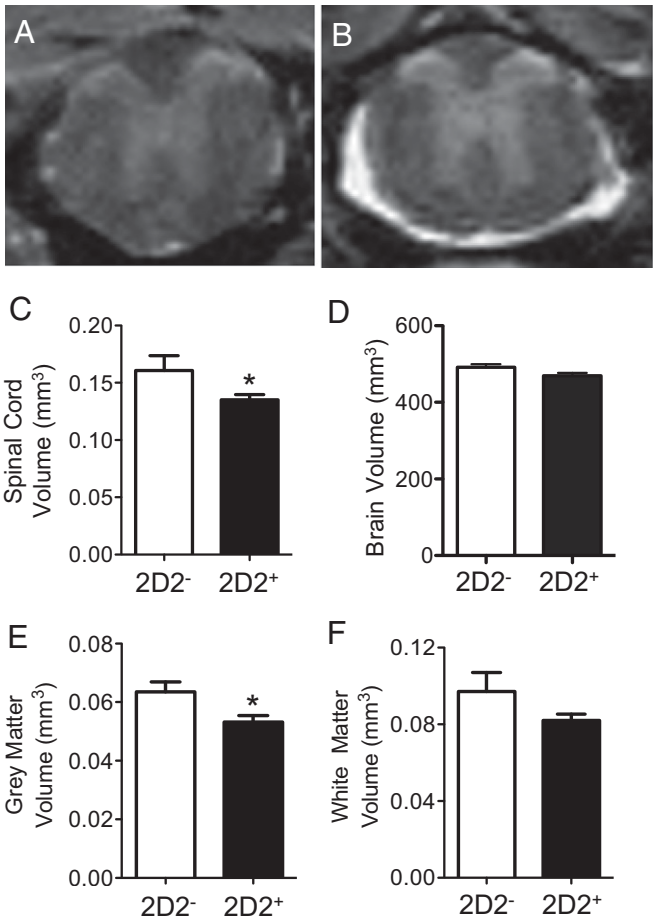

Fig. 5. Spinal cord atrophy is prominent in PPARα$^{mut/WT}$ 2D2^{+} mice with age as detected by MR. PPARα$^{mut/WT}$ 2D2^{+} females and sex-matched PPARα$^{mut/WT}$ 2D2^{-} littermates, aged 9 mo (n = 5 mice per group), were killed, and the spinal cord and brain specimens were fixed and imaged by MR. (*A* and *B*) Examples of MR images of the spinal cord in aged 2D2^{-} or 2D2^{+} mice. (*C*–*F*) Volumes of the whole spinal cord (*C*), the whole brain (*D*), spinal cord gray matter (*E*), and spinal cord white matter (*F*) in 2D2^{+} and 2D2^{-} mice. Means + SEM. *Significantly different from 2D2^{-} mice by Mann–Whitney *U* test (2-tailed) ($P \leq 0.05$).

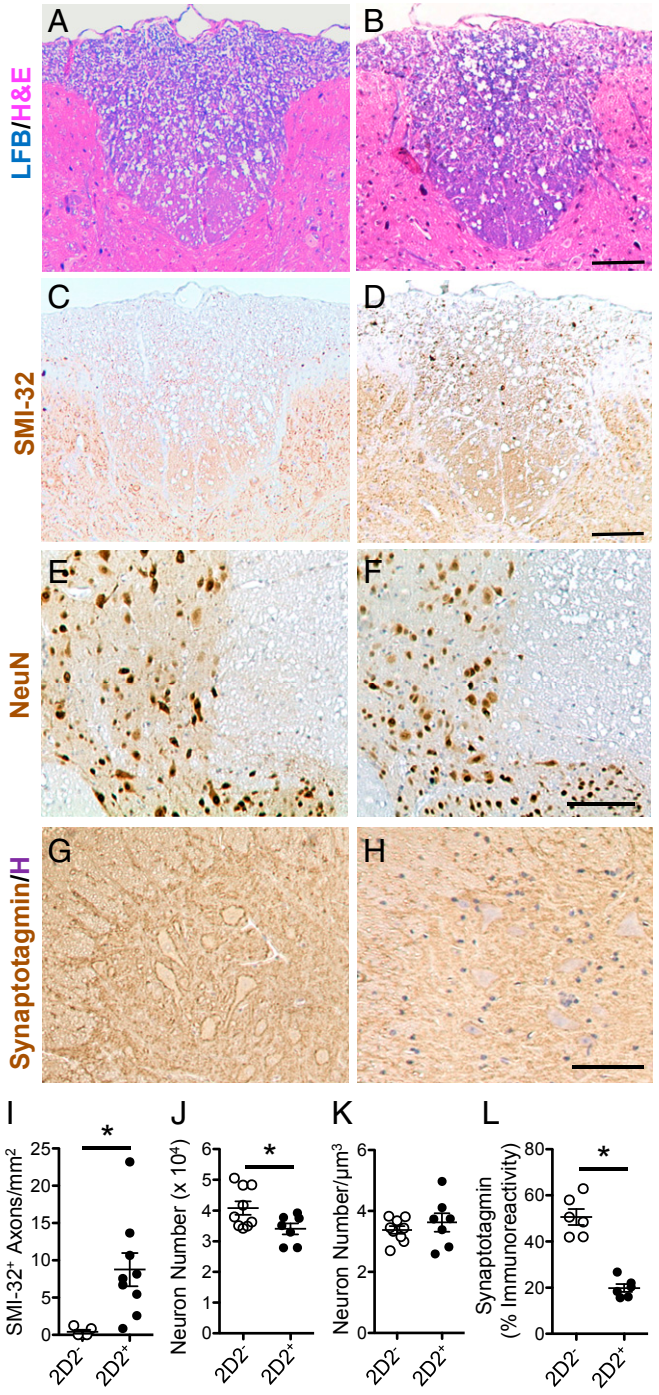

Fig. 6. White matter and gray matter pathology seen in long-term hind-limb clasping PPARα$^{mut/WT}$ 2D2^{+} mice. (*A–H*) Representative images of the posterior thoracic spinal cord white matter in aged PPARα$^{mut/WT}$ 2D2^{-} (*A*, *C*, *E*, and *G*) or PPARα$^{mut/WT}$ 2D2^{+} (*B*, *D*, *F*, and *H*) mice stained for LFB/H&E (*A* and *B*), SMI-32 (*C* and *D*), NeuN (*E* and *F*), or synaptotagmin (*G* and *H*). (Scale bars: *A–F*, 100 μm; *G* and *H*, 50 μm.) (*I–L*) Histology scoring for PPARα$^{mut/WT}$ 2D2^{+} and PPARα$^{mut/WT}$ 2D2^{-} mice. (*I*) SMI-32^{+} axons per square millimeter ($n = 9$ mice per group). (*J* and *K*) Number of NeuN^{+} nuclei in the gray matter determined using the optical fractionator method (*J*) and normalized per cubic micrometer tissue sampled (*K*; $n = 7$ 2D2^{+}, $n = 9$ 2D2^{-} mice per group). (*L*) Immunoreactivity for synaptotagmin in the gray matter of the spinal cord ($n = 6$ per group). In all cases, values are means ± SEM of values obtained in individual mice. Sample sizes differed according to stain since not all antibodies worked in all sections due to sample overfixation or decalcification. *Significantly different by Mann–Whitney *U* test (2-tailed) ($P \leq 0.05$).

absolute volume of 19 of the 62 brain structures in PPARα$^{mut/WT}$ 2D2^{+} mice (Table 2). Intriguingly, the extent of atrophy decreased as one moved rostrally in the brain, being highest in the medulla, followed by the pons, midbrain, and thalamus, with cortical and rostral areas of the brain being largely unaffected (Table 2 and Fig. 7). When examining specific tracts and nuclei, we observed atrophy in some of the brain structures that were inflamed earlier in life in PPARα$^{mut/WT}$ 2D2^{+} mice, including the optic tract, cerebral peduncle, and the inferior colliculus. In addition, certain nuclei that project axons to known inflamed sites were also atrophied, including the superior colliculus, which projects axons via the optic tract, and the pontine nucleus, which projects axons to the cerebellum. Volume loss was also evident in the corticospinal tract and along the posterior column–medial lemniscus pathway, including the cuneate nucleus, which receives input from neurons in the posterior spinal columns; the medial lemniscus tract, which conveys axons from the cuneate nucleus to the thalamus; and the thalamus. Together, these findings suggested that tissue loss occurred in the white matter tracts that were directly impacted by T cell-mediated inflammation and some nuclei associated with these sites, but also in specific structures that contained neurons that were in the same pathway but 1 to 2 synapses removed from affected tracts in the posterior spinal cord.

Discussion

Here, we observed that 2D2^{+} mice in our SPF colony presented with a prominent hind-limb clasping phenotype characterized by T cell infiltration in the posterior spinal cord and nerve roots. Because of the mild nature of the T cell inflammation and clinical signs, we decided to maintain cohorts of 2D2^{+} mice of a defined genotype (PPARα$^{mut/WT}$) into middle age. We observed that these mice exhibited relapsing-remitting course of hind-limb clasping and accumulated motor deficits with age. The disease progression with age appeared to be disconnected from T cell autoimmunity and more closely associated with atrophy of the spinal cord, neuron and axon loss, synapse degradation, and ongoing white matter injury. These findings suggest that hind-limb clasping EAE in 2D2^{+} mice has value as a model for SPMS.

The onset of hind-limb clasping in PPARα$^{mut/WT}$ 2D2^{+} mice associated with the presence of mild T cell infiltration, microglia activation, and axon injury in the posterior spinal cord and nerve roots. The exact cause of the hind-limb clasping reflex is not known; however, the location of the inflammatory lesions does coincide with past reports of this abnormal reflex in genetically altered strains of mice that exhibit axonopathy in motor or somatosensory pathways in the spinal cord, including the spinocerebellar projection pathway (27). Interestingly, this pathology differed from the pathology of classic EAE (in this study and other models) (12, 21, 43), where inflammation and axon injury are considerably more severe and affect ventral, lateral, and posterior aspects of the spinal cord. Our study did not resolve the immune mechanisms underpinning the dichotomous EAE presentation in PPARα$^{mut/WT}$ 2D2^{+} mice (hind-limb clasping vs. ascending paralysis); however, the observation that anti–NF-M T cell autoimmunity was dominant in this model (here and in ref. 31), coupled with past work that found that vaccination of mice with neurofilament light chain and CFA induces a T cell-mediated autoimmune disease that targets the dorsal spinal cord and nerve roots (44), point to the involvement of anti-NF autoimmunity in this disease. This concept could be further tested by examining whether this phenotype persists after crossing PPARα$^{mut/WT}$ 2D2^{+} mice onto an MOG-deficient background or disappears after crossing these mice onto an NF-M–deficient background.

We observed that hind-limb clasping in PPARα$^{mut/WT}$ 2D2^{+} mice became more persistent with age and associated with the accumulation of progressive motor deficits, reminiscent of SPMS and the progressive nature of clinical signs in certain EAE models

Table 2. Significant changes in absolute volume of brain structures that were significantly different in PPARα$^{mut/WT}$ 2D2^{+} (n = 5) compared to PPARα$^{mut/WT}$ 2D2^{-} mice (n = 5) at 9 mo of age

Structure	Change in absolute volume, %	Groupwise absolute volume differences uncorrected *P* value
Cerebellar peduncle: inferior	−8.9	0.0064***
Cerebellar peduncle: middle	−12.8	0.0082***
Cerebral peduncle	−8.8	0.0016***
Colliculus: inferior	−6.9	0.0012***
Colliculus: superior	−10.6	0.0012***
Corticospinal tract/pyramids	−6.7	0.041*
Cuneate nucleus	−12.5	0.00031****
Facial nerve (cranial nerve 7)	−11.3	0.0083***
Fasciculus retroflexus	−3.4	0.013**
Fimbria	−3.5	0.014**
Hypothalamus	−6.9	0.0082***
Mammillary bodies	−12.8	0.055*
Mammilothalamic tract	−6.1	0.00036****
Medial lemniscus/medial longitudinal fasciculus	−3.4	0.046*
Medial septum	−4.3	0.058*
Medulla	−9.1	0.00034****
Midbrain	−5.1	0.009***
Optic tract	−17.1	0.0016***
Pons	−8.5	0.0024***
Pontine nucleus	−16.8	0.025**
Posterior commissure	−5.5	0.052*
Stria medullaris	−5.0	0.0067***
Superior olivary complex	−9.3	0.055*
Thalamus	−5.6	0.006***
Third ventricle	−7.3	0.020**

The *P* values are marked with an asterisk (*) if that difference is significant at an FDR of 15%, 2 asterisks (**) for significant at an FDR of 10%, 3 asterisks (***) for significant at an FDR of 5%, and 4 asterisks (****) for significant at an FDR of 1%.

(45–47). In past EAE studies, neurological progression associated with cumulative axon loss in the spinal cord, including the major motor tracts (12, 46, 47). In contrast, in our study, progressive motor deficits associated with axon loss in the spinal cord, but also atrophy of the gray matter, the posterior–medial lemniscus pathway, and the corticospinal tract. The latter finding is consistent with the finding that small-diameter neurons in the corticospinal tract are vulnerable to injury in MS (48) and EAE (12, 46). Regarding the mechanisms of axonal injury, our TEM studies, which focused on dorsal spinal cord, indicated an increased frequency of collapsed myelin sheaths with absent axons, which points to a primary axonopathy. Interestingly, this type of pathology has been seen previously in chronic EAE (MOG p35-55/CFA-induced EAE) and in active lesions in MS (7). Consistent with these findings, in paraffin sections, we detected small numbers of SMI-32^{+} axons in the aged PPARα$^{mut/WT}$ 2D2^{+} mice. In sections where SMI-32^{+} axons were more abundant, microglia in adjacent sections displayed an activated morphology, reminiscent of white matter pathology in long-term chronic EAE (12) and progressive MS (49, 50). Though activated microglia are considered to contribute to neuronal injury in MS (3), it is unclear whether microglia are reacting to, or contributing to, axon injury in our model.

Though the extent of the loss (−25%) of axons in the spinal cord white matter in PPARα$^{mut/WT}$ 2D2^{+} mice with age was less extensive than that seen in young mice in classic EAE models (−60 to −66%) (21, 46, 47) or in postmortem studies in MS (−40 to −70%) (48, 51, 52), the gray matter pathology was comparable or even more extensive. For example, the extent of spinal cord gray matter atrophy was equivalent to that seen in mice after 100 d of MOG p35-55/CFA-induced EAE, which presents as a much more severe disease (53). The extent of total spinal cord atrophy in our model was also similar to that reported for humans 20 y out from diagnosis of relapsing-remitting MS (54–56). The loss in gray matter volume in our study associated with a loss in neuronal perikarya, which contrasts with findings in long-term (100 d) chronic EAE where atrophy instead associated with a loss in size of perikarya and dendrite thinning (53). Though we did not evaluate neuronal dendrite morphology in our study, we did stain for a synaptic marker and observed a significant reduction in synaptotagmin-positive synapses in the spinal cord gray matter in the aged PPARα$^{mut/WT}$ 2D2^{+} mice. Past studies in EAE reported decreased synaptic staining in the gray matter during the acute phase of EAE, but this staining reversed to naïve control levels in postacute phase of disease after inflammation had subsided (57). Our findings are therefore more in line with observations of persistent synaptic loss seen in the demyelinated hippocampus and cortical lesions in progressive MS (39, 40, 58).

Beyond these pathology findings, we observed a number of other striking parallels between hind-limb clasping EAE seen in PPARα$^{mut/WT}$ 2D2^{+} mice and relapsing-remitting MS. Similar to findings in MS (59, 60), clinical signs in 2D2^{+} mice were more frequent in females than males, abated in late pregnancy, and reemerged postpartum. We also observed that the TCR transgenic cells expressed IFN-γ or coproduced IFN-γ and GM-CSF, which is consistent with findings that these Th subsets are overrepresented in the circulation of MS patients (61). In addition, autoantibodies of the IgG1 isotype were detected in PPARα$^{mut/WT}$ 2D2^{+} mice, which is also described in MS (36). Finally, T cell autoimmune attacks became more sporadic in PPARα$^{mut/WT}$ 2D2^{+} mice with age, resembling the situation in MS patients with long-standing disease, where inflammatory infiltrates decline to levels seen in age-matched controls (4). Together, these findings underscore the utility of EAE in modeling the effects of sex, hormones, and natural aging on T cell autoimmune mechanisms in MS.

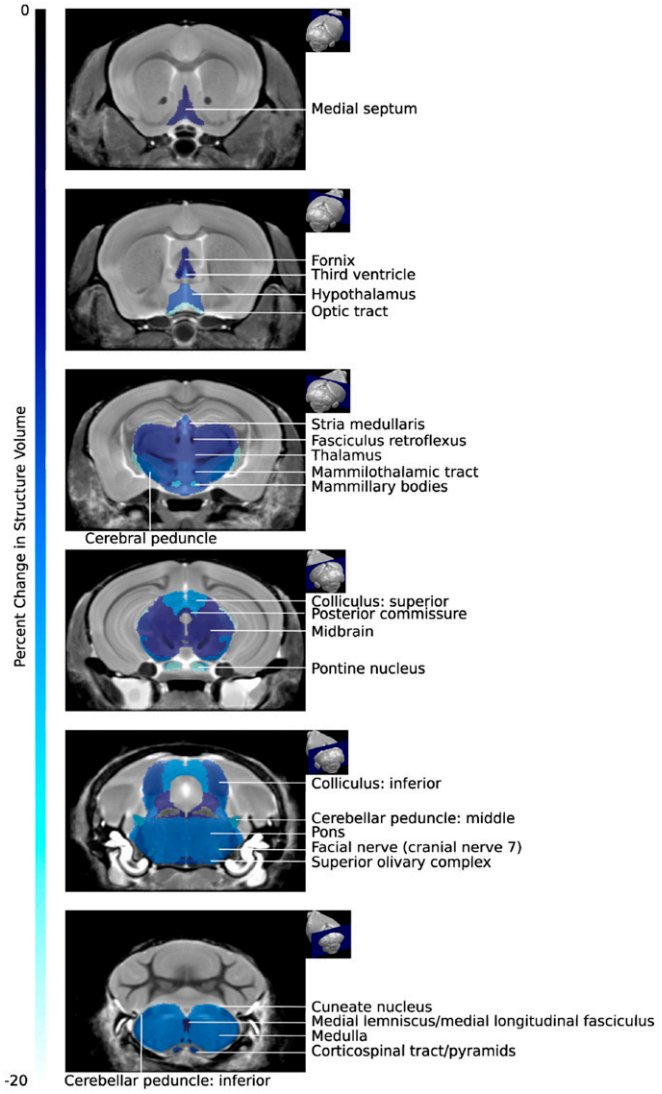

Fig. 7. Atrophy was prominent in certain brain structures that were directly impacted by inflammation or were in close proximity to the spinal cord. Coronal MRI slices showing the differences in absolute structure volume between PPARα$^{mut/WT}$ 2D2^{+} and PPARα$^{mut/WT}$ 2D2^{-} mice (FDR 10%). Slices arranged from the anterior (*Top*) to posterior (*Bottom*). The percentage change in brain structure volume is indicated by the color scale bar shown on the left.

Despite these similarities, hind-limb clasping EAE mice do not capture all of the pathological features of human MS. For example, aged PPARα$^{mut/WT}$ 2D2^{+} mice did not exhibit signs of extensive chronic demyelination, which is a hallmark of progressive MS and has been noted in other EAE models (46). Though submeningeal immune cell infiltrates with B and T cell clusters were seen in a few young PPARα$^{mut/WT}$ 2D2^{+} mice with hind-limb clasping, this process was infrequent with age, contrasting with findings in SPMS, where submeningeal inflammation is present in 40% of patients (62). We also did not observe IgG deposition in the CNS, which is a hallmark of pattern II lesions in MS (63).

A limitation of our study is that we only conducted MR studies at endpoint and provided only 2 temporal snapshots of the pathology in PPARα$^{mut/WT}$ 2D2^{+} mice. Longitudinal MRI studies of live 2D2^{+} mice coupled with timed T or B cell depletion therapy and histopathological studies at endpoint would certainly help better pinpoint the contribution of autoimmune processes to the neuronal injury. A barrier limiting the widespread use of this or other spontaneous EAE models is that disease presents differently in individual SPF facilities (24, 64). We speculate that the increased penetrance of classic EAE in 2D2^{+} mice in our facility related to the microbiota of the original 2D2^{+} breeders from Jackson Laboratory, since this phenotype was present in the parental 2D2^{+} colony established in 2009 and remained stable until 2017, when we attempted to regenerate our 2D2^{+} colony by crossing fresh C57BL6/J females with in-house 2D2^{+} males (i.e., mothers provide the major initial source of microbiota for pups). Nonetheless, our observations here, coupled with descriptions of similar mild, nonclassical EAE presentations in this and other myelin-specific TCR transgenic strains (20, 64), underscore the utility of TCR transgenic mice to model the effect of natural aging on EAE-induced neurodegeneration.

Materials and Methods

Mice. Breeder pairs of 2D2^{+} mice on the C57BL6/J background were purchased from the Jackson Laboratory. Breeder pairs of PPARα$^{mut/mut}$ mice (model *Ppara*) were purchased from Taconic Farms. Offspring from these breeders were intercrossed to generate heterozygotes for 2D2 and PPARα transgenes (PPARα$^{mut/WT}$). F1 mice were crossed to generate PPARα$^{WT/WT}$, PPARα$^{mut/WT}$, and PPARα$^{mut/mut}$ 2D2^{+} F2 offspring. Offspring from the parental 2D2^{+} colony and F1 and F2 generations were followed for the development of clinical signs for 20 wk. After this, PPARα$^{mut/WT}$ F2 2D2^{+} mice were intercrossed to maintain the line for characterization of the hind-limb clasping phenotype. Additional studies were conducted on cohorts of female PPARα$^{mut/WT}$ 2D2^{+} and littermate PPARα$^{mut/WT}$ controls that did not express the 2D2 transgene. Mice were housed under SPF conditions, and all experiments were approved by the University Health Network Animal Care Committee following the guidelines established by the Canadian Council of Animal Care.

Clinical Scoring of Classic EAE and Hind-limb Clasping-Onset EAE. Mice that developed classical EAE signs were scored for the severity of ascending paralysis where 0 indicated no clinical signs, 1 indicated tail paralysis, 2 indicated hind limb or foot weakness, 3 indicated hind-limb paralysis in one or both hind limbs, 4 indicated some forelimb weakness, and 5 indicated moribund or death. In initial studies where we followed parental, F1, and F2 2D2^{+} mice for clinical scores, only the presence or absence of hind-limb clasping was noted. In subsequent studies, we developed a scoring scale to capture hind-limb clasping and foot weakness: 0 indicated normal splaying of hind limbs and no evidence of foot weakness, 1 indicated transient clasping of 1 hind limb, 2 indicated transient clasping of 2 hind limbs, 3 indicated severe and sustained hind limb clasping with dystonia, and 4 indicated hind limb clasping in one or both limbs plus foot weakness while walking across a wire cage top.

Ex Vivo MR Imaging. Mice were killed using a transcardiac perfusion with 2 mM ProHance (Bracco Diagnostics) as described in detail previously (65). After perfusion, mice were decapitated, and the skull containing the brains and the spinal column was dissected and stored in 4% PFA containing 2 mM ProHance overnight at 4 °C and then transferred to PBS containing 2 mM ProHance and 0.02% sodium azide. The spinal cord tissue was further divided into ~2-cm sections for imaging. A 16-coil solenoid array was used to image 16 samples concurrently using a 7.0-T magnet (Varian). A T2-weighted 3D fast spin-echo sequence was used to acquire anatomical images: TR, 2,000 ms; echo train length, 6; TE_{eff}, 42 ms; field of view, 25 × 28 × 14 mm; and matrix size, 450 × 504 × 250, producing an image with an isotropic resolution of 56 μm.

Volume Analysis. To determine spinal cord volume, the gray and white matter was manually segmented in 3D using the Amira software package (Visage Imaging). The same number of vertebrae were segmented for each image and the volume normalized to the number of MR slices (66). To assess anatomical differences in brain morphology, an automated image registration-based approach using the Advanced Normalization deformation algorithm (67) was used. The images were registered together using linear and nonlinear steps to form an average image (68). The registration yielded deformation fields for each individual brain, which were then used to calculate an estimate of local volume change at every voxel (69). A segmented atlas with 62 labeled structures (70) was registered to the average image to calculate the volume of the brain structures in each image.

Statistics. The proportion of mice displaying EAE or clasping symptoms was analyzed between groups using χ^2 test. The severity of clinical symptoms and immune and histological measures were compared between groups using a 2-tailed *t* test (2 groups, parametric), 2-tailed Mann–Whitney *U* test (2 groups, nonparametric data), a 1-way ANOVA (3 groups, parametric), or Kruskal–Wallis test (3 groups, nonparametric). RMINC (https://github.com/Mouse-Imaging-Centre/RMINC) and R statistical software (www.r-project.org) were used to analyze MR data. Data from each group of animals are reported as mean ± SEM. For the MR volumetric data, a 2-tailed *t* test was computed for each structure and at every voxel. A correction for multiple comparisons was performed with a false discovery rate (FDR) (71) of, at most, 10%.

Details of mouse genotyping, rotarod and grip testing, histopathological analyses, stereological analysis, and immune studies are provided in *SI Appendix, Supplementary Methods*.

ACKNOWLEDGMENTS. We thank Dr. Jonathon Brotchie for the use of the Rotarod device, Dr. Guy Higgins (CanCog) for sharing protocols for rotarod and neurological scoring, Audrey Darabie and Yan Chen for help with TEM studies, Dr. Kevin Conway (Advanced Microscopy Facility, Toronto Western Hospital) for training in stereology analysis, Dr. Daniel Winer for histological advice, and Dr. Andrzej Chruscinski for providing the positive control tissue for Ig staining. This study was funded by a Don Paty award and operating grant from the MS Society of Canada (to S.E.D.) and MS Society studentships (to M.A.Z. and F.L.Z.).

1. A. J. Thompson, S. E. Baranzini, J. Geurts, B. Hemmer, O. Ciccarelli, Multiple sclerosis. *Lancet* **391**, 1622–1636 (2018).
2. J. M. Frischer *et al.*, Clinical and pathological insights into the dynamic nature of the white matter multiple sclerosis plaque. *Ann. Neurol.* **78**, 710–721 (2015).
3. D. H. Mahad, B. D. Trapp, H. Lassmann, Pathological mechanisms in progressive multiple sclerosis. *Lancet Neurol.* **14**, 183–193 (2015).
4. J. M. Frischer *et al.*, The relation between inflammation and neurodegeneration in multiple sclerosis brains. *Brain* **132**, 1175–1189 (2009).
5. L. Haider *et al.*, Oxidative damage in multiple sclerosis lesions. *Brain* **134**, 1914–1924 (2011).
6. C. Bjartmar, B. D. Trapp, Axonal degeneration and progressive neurologic disability in multiple sclerosis. *Neurotox. Res.* **5**, 157–164 (2003).
7. I. Nikić *et al.*, A reversible form of axon damage in experimental autoimmune encephalomyelitis and multiple sclerosis. *Nat. Med.* **17**, 495–499 (2011).
8. N. Evangelou *et al.*, Size-selective neuronal changes in the anterior optic pathways suggest a differential susceptibility to injury in multiple sclerosis. *Brain* **124**, 1813–1820 (2001).
9. M. T. Fischer *et al.*, NADPH oxidase expression in active multiple sclerosis lesions in relation to oxidative tissue damage and mitochondrial injury. *Brain* **135**, 886–899 (2012).
10. I. Gabilondo *et al.*, Trans-synaptic axonal degeneration in the visual pathway in multiple sclerosis. *Ann. Neurol.* **75**, 98–107 (2014).
11. N. B. Pikor *et al.*, Integration of Th17- and lymphotoxin-derived signals initiates meningeal-resident stromal cell remodeling to propagate neuroinflammation. *Immunity* **43**, 1160–1173 (2015).
12. A. M. Soulika *et al.*, Initiation and progression of axonopathy in experimental autoimmune encephalomyelitis. *J. Neurosci.* **29**, 14965–14979 (2009).
13. M. Kipp, S. Nyamoya, T. Hochstrasser, S. Amor, Multiple sclerosis animal models: A clinical and histopathological perspective. *Brain Pathol.* **27**, 123–137 (2017).
14. I. M. Stromnes, J. M. Goverman, Active induction of experimental allergic encephalomyelitis. *Nat. Protoc.* **1**, 1810–1819 (2006).
15. J. Goverman *et al.*, Transgenic mice that express a myelin basic protein-specific T cell receptor develop spontaneous autoimmunity. *Cell* **72**, 551–560 (1993).
16. E. Bettelli *et al.*, Myelin oligodendrocyte glycoprotein-specific T cell receptor transgenic mice develop spontaneous autoimmune optic neuritis. *J. Exp. Med.* **197**, 1073–1081 (2003).
17. B. Pöllinger *et al.*, Spontaneous relapsing-remitting EAE in the SJL/J mouse: MOG-reactive transgenic T cells recruit endogenous MOG-specific B cells. *J. Exp. Med.* **206**, 1303–1316 (2009).
18. E. Bettelli, D. Baeten, A. Jäger, R. A. Sobel, V. K. Kuchroo, Myelin oligodendrocyte glycoprotein-specific T and B cells cooperate to induce a Devic-like disease in mice. *J. Clin. Invest.* **116**, 2393–2402 (2006).
19. G. Krishnamoorthy, H. Lassmann, H. Wekerle, A. Holz, Spontaneous opticospinal encephalomyelitis in a double-transgenic mouse model of autoimmune T cell/B cell cooperation. *J. Clin. Invest.* **116**, 2385–2392 (2006).
20. S. Ellmerich *et al.*, Disease-related epitope spread in a humanized T cell receptor transgenic model of multiple sclerosis. *Eur. J. Immunol.* **34**, 1839–1848 (2004).
21. M. V. Jones *et al.*, Behavioral and pathological outcomes in MOG 35-55 experimental autoimmune encephalomyelitis. *J. Neuroimmunol.* **199**, 83–93 (2008).
22. S. E. Dunn *et al.*, Peroxisome proliferator-activated receptor (PPAR)alpha expression in T cells mediates gender differences in development of T cell-mediated autoimmunity. *J. Exp. Med.* **204**, 321–330 (2007).
23. D. Dubey *et al.*, PDCB does not promote CNS autoimmunity in the context of genetic susceptibility but worsens its outcome. *J. Neuroimmunol.* **323**, 53–55 (2018).
24. K. Berer *et al.*, Commensal microbiota and myelin autoantigen cooperate to trigger autoimmune demyelination. *Nature* **479**, 538–541 (2011).
25. M. Gharagozloo *et al.*, The dual immunoregulatory function of *Nlrp12* in T cell-mediated immune response: Lessons from experimental autoimmune encephalomyelitis. *Cells* **7**, E119 (2018).
26. U. Schulze-Topphoff *et al.*, Tob1 plays a critical role in the activation of encephalitogenic T cells in CNS autoimmunity. *J. Exp. Med.* **210**, 1301–1309 (2013).
27. R. Lalonde, C. Strazielle, Brain regions and genes affecting limb-clasping responses. *Brain Res. Brain Res. Rev.* **67**, 252–259 (2011).
28. E. R. Pierson, I. M. Stromnes, J. M. Goverman, B cells promote induction of experimental autoimmune encephalomyelitis by facilitating reactivation of T cells in the central nervous system. *J. Immunol.* **192**, 929–939 (2014).
29. C. Römer *et al.*, Blocking stroke-induced immunodeficiency increases CNS antigen-specific autoreactivity but does not worsen functional outcome after experimental stroke. *J. Neurosci.* **35**, 7777–7794 (2015).
30. M. Varrin-Doyer *et al.*, Treatment of spontaneous EAE by laquinimod reduces Tfh, B cell aggregates, and disease progression. *Neurol. Neuroimmunol. Neuroinflamm.* **3**, e272 (2016).
31. G. Krishnamoorthy *et al.*, Myelin-specific T cells also recognize neuronal autoantigen in a transgenic mouse model of multiple sclerosis. *Nat. Med.* **15**, 626–632 (2009).
32. G. Schönrich *et al.*, Down-regulation of T cell receptors on self-reactive T cells as a novel mechanism for extrathymic tolerance induction. *Cell* **65**, 293–304 (1991).
33. B. Rocha, H. von Boehmer, Peripheral selection of the T cell repertoire. *Science* **251**, 1225–1228 (1991).
34. X. Montalban, S. Belachew, J. S. Wolinsky, Ocrelizumab in primary progressive and relapsing multiple sclerosis. *N. Engl. J. Med.* **376**, 1694 (2017).
35. H. Lassmann, Pathogenic mechanisms associated with different clinical courses of multiple sclerosis. *Front. Immunol.* **9**, 3116 (2019).
36. F. Di Pauli, T. Berger, Myelin oligodendrocyte glycoprotein antibody-associated disorders: Toward a new spectrum of inflammatory demyelinating CNS disorders? *Front. Immunol.* **9**, 2753 (2018).
37. H. J. Gundersen, Stereology of arbitrary particles. A review of unbiased number and size estimators and the presentation of some new ones, in memory of William R. Thompson. *J. Microsc.* **143**, 3–45 (1986).
38. M. J. West, L. Slomianka, H. J. Gundersen, Unbiased stereological estimation of the total number of neurons in thesubdivisions of the rat hippocampus using the optical fractionator. *Anat. Rec.* **231**, 482–497 (1991).
39. I. Michailidou *et al.*, Complement C1q-C3-associated synaptic changes in multiple sclerosis hippocampus. *Ann. Neurol.* **77**, 1007–1026 (2015).
40. C. Wegner, M. M. Esiri, S. A. Chance, J. Palace, P. M. Matthews, Neocortical neuronal, synaptic, and glial loss in multiple sclerosis. *Neurology* **67**, 960–967 (2006).
41. L. Kappos *et al.*; EXPAND Clinical Investigators, Siponimod versus placebo in secondary progressive multiple sclerosis (EXPAND): A double-blind, randomised, phase 3 study. *Lancet* **391**, 1263–1273 (2018).
42. A. Gentile *et al.*, Siponimod (BAF312) prevents synaptic neurodegeneration in experimental multiple sclerosis. *J. Neuroinflammation* **13**, 207 (2016).
43. J. L. Berard, B. J. Kerr, H. M. Johnson, S. David, Differential expression of SOCS1 in macrophages in relapsing-remitting and chronic EAE and its role in disease severity. *Glia* **58**, 1816–1826 (2010).
44. R. Huizinga *et al.*, Immunization with neurofilament light protein induces spastic paresis and axonal degeneration in Biozzi ABH mice. *J. Neuropathol. Exp. Neurol.* **66**, 295–304 (2007).
45. G. Pryce *et al.*, Autoimmune tolerance eliminates relapses but fails to halt progression in a model of multiple sclerosis. *J. Neuroimmunol.* **165**, 41–52 (2005).
46. S. J. Jackson, J. Lee, M. Nikodemova, Z. Fabry, I. D. Duncan, Quantification of myelin and axon pathology during relapsing progressive experimental autoimmune encephalomyelitis in the Biozzi ABH mouse. *J. Neuropathol. Exp. Neurol.* **68**, 616–625 (2009).
47. J. R. Wujek *et al.*, Axon loss in the spinal cord determines permanent neurological disability in an animal model of multiple sclerosis. *J. Neuropathol. Exp. Neurol.* **61**, 23–32 (2002).
48. P. Ganter, C. Prince, M. M. Esiri, Spinal cord axonal loss in multiple sclerosis: A post-mortem study. *Neuropathol. Appl. Neurobiol.* **25**, 459–467 (1999).
49. A. Kutzelnigg *et al.*, Cortical demyelination and diffuse white matter injury in multiple sclerosis. *Brain* **128**, 2705–2712 (2005).
50. J. van Horssen *et al.*, Clusters of activated microglia in normal-appearing white matter show signs of innate immune activation. *J. Neuroinflammation* **9**, 156 (2012).
51. N. Evangelou, G. C. DeLuca, T. Owens, M. M. Esiri, Pathological study of spinal cord atrophy in multiple sclerosis suggests limited role of local lesions. *Brain* **128**, 29–34 (2005).
52. G. C. DeLuca, G. C. Ebers, M. M. Esiri, Axonal loss in multiple sclerosis: A pathological survey of the corticospinal and sensory tracts. *Brain* **127**, 1009–1018 (2004).
53. P. G. Bannerman *et al.*, Motor neuron pathology in experimental autoimmune encephalomyelitis: Studies in THY1-YFP transgenic mice. *Brain* **128**, 1877–1886 (2005).
54. M. A. Rocca *et al.*, A multicenter assessment of cervical cord atrophy among MS clinical phenotypes. *Neurology* **76**, 2096–2102 (2011).
55. R. Zivadinov *et al.*, Comparison of three different methods for measurement of cervical cord atrophy in multiple sclerosis. *AJNR Am. J. Neuroradiol.* **29**, 319–325 (2008).
56. A. Gass *et al.*; MAGNIMS Study Group, MRI monitoring of pathological changes in the spinal cord in patients with multiple sclerosis. *Lancet Neurol.* **14**, 443–454 (2015).
57. B. Zhu, L. Luo, G. R. Moore, D. W. Paty, M. S. Cynader, Dendritic and synaptic pathology in experimental autoimmune encephalomyelitis. *Am. J. Pathol.* **162**, 1639–1650 (2003).
58. R. Dutta *et al.*, Demyelination causes synaptic alterations in hippocampi from multiple sclerosis patients. *Ann. Neurol.* **69**, 445–454 (2011).

59. S. E. Dunn, H. Lee, F. R. Pavri, M. A. Zhang, Sex-based differences in multiple sclerosis (Part I): Biology of disease incidence. *Curr. Top. Behav. Neurosci.* **26**, 29–56 (2015).
60. C. Confavreux, M. Hutchinson, M. M. Hours, P. Cortinovis-Tourniaire, T. Moreau; Pregnancy in Multiple Sclerosis Group, Rate of pregnancy-related relapse in multiple sclerosis. *N. Engl. J. Med.* **339**, 285–291 (1998).
61. F. J. Hartmann *et al*., Multiple sclerosis-associated IL2RA polymorphism controls GM-CSF production in human TH cells. *Nat. Commun.* **5**, 5056 (2014).
62. R. Magliozzi *et al*., Meningeal B-cell follicles in secondary progressive multiple sclerosis associate with early onset of disease and severe cortical pathology. *Brain* **130**, 1089–1104 (2007).
63. C. Lucchinetti *et al*., Heterogeneity of multiple sclerosis lesions: Implications for the pathogenesis of demyelination. *Ann. Neurol.* **47**, 707–717 (2000).
64. Y. Laouar *et al*., TGF-beta signaling in dendritic cells is a prerequisite for the control of autoimmune encephalomyelitis. *Proc. Natl. Acad. Sci. U.S.A.* **105**, 10865–10870 (2008).
65. L. S. Cahill *et al*., Preparation of fixed mouse brains for MRI. *Neuroimage* **60**, 933–939 (2012).
66. B. C. Healy *et al*., Approaches to normalization of spinal cord volume: Application to multiple sclerosis. *J. Neuroimaging* **22**, e12–e19 (2012).
67. B. B. Avants, C. L. Epstein, M. Grossman, J. C. Gee, Symmetric diffeomorphic image and registration with cross-correlation: Evaluating automated labeling of elderly and neurodegenerative brain. *Med. Image Anal.* **12**, 26–41 (2008).
68. J. P. Lerch, J. G. Sled, R. M. Henkelman, MRI phenotyping of genetically altered mice. *Methods Mol. Biol.* **711**, 349–361 (2011).
69. M. K. Chung *et al*., A unified statistical approach to deformation-based morphometry. *Neuroimage* **14**, 595–606 (2001).
70. A. E. Dorr, J. P. Lerch, S. Spring, N. Kabani, R. M. Henkelman, High resolution three-dimensional brain atlas using an average magnetic resonance image of 40 adult C57Bl/6J mice. *Neuroimage* **42**, 60–69 (2008).
71. C. R. Genovese, N. A. Lazar, T. Nichols, Thresholding of statistical maps in functional neuroimaging using the false discovery rate. *Neuroimage* **15**, 870–878 (2002).